

# Versatile Synthesis of Nanofoams through Femtosecond Pulsed Laser Deposition

Davide Orecchia,\* Alessandro Maffini,\* Margherita Zavelani-Rossi, and Matteo Passoni

Nanofoam materials are gaining increasing interest in the scientific community, thanks to their unique properties such as ultralow density, complex nano- and microstructure, and high surface area. Nanofoams are attractive for multiple applications, ranging from advanced catalysis and energy storage to nuclear fusion and particle acceleration. The main issues hindering the widespread use of nanofoams are related to the choice of synthesis technique, highly dependent on the desired elemental composition and leading to a limited control over the main material properties. Herein, femtosecond pulsed laser deposition is proposed as a universal tool for the synthesis of nanofoams with tailored characteristics. Nanofoams made by elements with significantly different properties—namely, boron, silicon, copper, tungsten, and gold—can be produced by suitably tuning the deposition parameters. The effect of the background pressure is studied in detail, in relation to the morphological features and density of the resulting nanofoams and nanostructured films. This, together with the analysis of the specific features shown by nanofoams made of different elements, offers fresh insights into the aggregation process and its relation to the corresponding nanofoam properties down to the nanoscale, opening new perspectives toward the application of nanofoam-based materials.

and nanometric scale. Among the most interesting attributes of nanofoams is their low mass density, typically falling within the range of  $1\text{--}100\text{ mg cm}^{-3}$ . This, in combination with a very high surface-to-volume ratio, makes nanofoams interesting for a broad range of applications, including supercapacitor devices,<sup>[1,2]</sup> energy storage,<sup>[3,4]</sup> hydrogen storage,<sup>[5,6]</sup> advanced catalysis,<sup>[7,8]</sup> solar energy conversion,<sup>[9,10]</sup> pollutant removal,<sup>[11,12]</sup> gas sensing,<sup>[13,14]</sup> and nanomedicine.<sup>[15,16]</sup> In the past years, nanofoams have been studied as effective enhancers in high-intensity laser-matter interaction<sup>[17]</sup> for laser-driven ion acceleration,<sup>[18–21]</sup> neutron<sup>[22]</sup> and radioisotopes generation,<sup>[23]</sup> and inertial confinement fusion.<sup>[24–26]</sup> Moreover, nanofoams can serve as model materials for fundamental nanotechnology research. Scientists study their unique properties and behavior to gain insights into nanoscale phenomena, which can lead to further advancements in materials science.


## 1. Introduction

Nanofoam is a class of nanostructured materials characterized by a disordered and porous structure, featuring a substantial volume fraction of submicrometric voids and pores, typically exceeding 90% of their volume. Nanofoams have attracted growing attention within the scientific community due to remarkable properties that are related to their structure at the micrometric

Taking into consideration the ample range of different applications, the interest in producing nanofoam with different properties is clear. For instance, the nanofoam composition is fundamental when chemical or nuclear reactions are involved. The desired density can also vary, and the same can be said for the nanofoam morphology: it can range from solid materials with voids to bottom-up fiber-assembled or nanoparticle-assembled structures. For all these reasons, a single technique able to produce nanofoams with controlled properties, and different materials, is of certain interest. Various techniques have been employed for the synthesis of nanofoams, each one being usually suited for specific combinations of elements, morphologies, and average density ranges: chemical vapor deposition (CVD),<sup>[27–29]</sup> thermal evaporation for metallic foams,<sup>[30]</sup> sol-gel method for silica nanofoams,<sup>[31]</sup> CO<sub>2</sub> foaming processes<sup>[32]</sup> for polymer nanofoams, and aerosol-assisted chemical vapor deposition for ceramic nanofoams.<sup>[33]</sup> Among these methods, pulsed laser deposition (PLD) stands out as a versatile and promising tool for nanofoam synthesis. PLD versatility can be exploited to fine tune material properties by acting on the main process parameters, such as laser wavelength, pulse energy and fluence, pulse duration, composition and pressure of background atmosphere, target-to-substrate distance, and overall geometry of the deposition system. Notably, its flexibility is extended to the material composition, and nanofoams of different elements can be produced with the same technique.

D. Orecchia, A. Maffini, M. Zavelani-Rossi, M. Passoni  
Energy Department  
Politecnico di Milano  
via G. Ponzio 34/3, 20133 Milano, Italy  
E-mail: davide.orecchia@polimi.it; alessandro.maffini@polimi.it

M. Zavelani-Rossi  
Istituto di Fotonica e Nanotecnologie  
Consiglio Nazionale delle Ricerche  
piazza Leonardo da Vinci 32, 20133 Milano, Italy

 The ORCID identification number(s) for the author(s) of this article can be found under <https://doi.org/10.1002/ssstr.202300560>.

© 2024 The Authors. Small Structures published by Wiley-VCH GmbH. This is an open access article under the terms of the Creative Commons Attribution License, which permits use, distribution and reproduction in any medium, provided the original work is properly cited.

DOI: 10.1002/ssstr.202300560

As a relevant example, gold nanofoams for catalytic applications,<sup>[34]</sup> tungsten oxide nanofoams for gas sensing,<sup>[35]</sup> and carbon nanofoams for laser-driven particle acceleration<sup>[20,36]</sup> were all synthesized with the same PLD system in our laboratory based on a nanosecond pulsed laser. Nevertheless, the conventional nanosecond pulsed laser deposition (ns-PLD) technique is not without limitations, such as the presence of micrometric droplets (due to melting of the target surface), the necessity of a background pressure in order to produce nanoparticles (since the ablated species are atoms and ions), and the difficulty of ablating certain classes of materials (for which lower laser wavelength and/or higher fluence may be required).

In this regard, the less explored approach of femtosecond pulsed laser deposition (fs-PLD) is of particular interest. Due to the short timescale of the laser energy deposition (femtoseconds), faster than the ion reticle relaxation time (nanoseconds), the ultrafast ablation mechanism is electronic in nature.<sup>[37,38]</sup> No or limited heating of the target material occurs, while clusters and nanoparticles can be emitted directly.<sup>[39,40]</sup> Picosecond lasers share many of the features of ultrafast ablation, such as direct nanoparticle emission, but the material removal efficiency is lower for pulse durations higher than the mechanical expansion time, that is, a few picoseconds.<sup>[41]</sup> By virtue of their convenient features, femtosecond lasers are widely exploited in surface treatment and micro/nanostructuring of materials.<sup>[42–46]</sup> In the context of fs-PLD and nanofoam production, the femtosecond laser ablation features are especially interesting for multiple reasons: the nanoparticles—which are the basic building blocks of nanofoam materials—are readily available, and the absence of heating and melting can reduce unwanted film contaminations from droplets, one of the main issues observed in ns-PLD produced films. Moreover, not requiring heating and vaporization of the target during the ablation process, fs-PLD allows greater flexibility in target material choice: materials with substantially different properties can be efficiently ablated under the same laser conditions (fluence and wavelength), opening the possibility of simultaneous codepositions of different materials to grow composite films. The reduced dependence of the ultrafast ablation process on material properties leads also to the possibility of preserving the target stoichiometry in the produced materials.<sup>[47,48]</sup> Finally, considering the subset of materials and films that can be obtained through either nanosecond, picosecond, or femtosecond PLD, investigating the pulse duration as an additional PLD process parameter remains worthwhile: it leads to an increased flexibility in controlling the properties of the produced nanostructured films, by choosing the best technique depending on the desired outcome.

In previous works, we focused our attention on carbon, due to the intrinsic interest and widespread applications of carbon-based materials. We studied the synthesis of carbon nanofoams using both ns-PLD and fs-PLD.<sup>[36,49–51]</sup> We have elucidated the dynamics of carbon nanoparticle aggregation into a nanofoam and the evolution of nanofoam morphology in ns-PLD by means of a *snowfall model*.<sup>[49]</sup> the ablated species, expanding in a gas background, cool down and condensate in form of nanoparticles; these nanoparticles coalesce into micrometric fractal-like aggregates through a process described by the cluster–cluster aggregation mechanism. The aggregates then land onto the substrate producing the porous, connected web-like structure typical

of nanofoams. Moreover, we have assessed the relationship between nanofoam properties at the nanoscale (e.g., nanoparticle size, gyration radius of fractal-like aggregates, and their fractal dimension) and at the macroscopic scale (such as average density and uniformity) in both ns-PLD and fs-PLD, highlighting the peculiarities of each deposition regime.<sup>[51]</sup>

Nevertheless, the versatility of PLD comes with inherent complexities. Indeed, the relationship between process parameters and resulting material properties is in general not straightforward. Furthermore, the set of optimal parameters required to grow a nanofoam is inherently material dependent. This implies that achieving nanofoams for a broad range of materials is far from obvious.

These results laid the foundation for a more comprehensive investigation on PLD synthesis of nanofoam, exploring a wide range of elements of potential interest in the view of applications, from basic research to emerging technologies. In particular, in this work, we assess the potential of fs-PLD as a universal tool for the synthesis of nanofoams with tailored properties across a diverse array of materials, with a wide range of properties. From this point of view, the aim is to consider both metals and semiconductors, high-Z and low-Z elements, with a range of densities and melting temperatures. Secondly, the material choices are influenced by potential applications, with a specific focus on our research activities: boron nanofoams are of interest for laser-driven proton–boron fusion,<sup>[52]</sup> gold nanofoams for X-ray generation in indirect drive inertial confinement fusion,<sup>[53]</sup> gold and copper as catalytic materials,<sup>[34,54]</sup> tungsten for plasma–matter interaction studies relevant in magnetic confinement fusion.<sup>[55]</sup> Finally, precedence is given to materials for which the conventional ns-PLD approach is challenging or not feasible, especially in relation to the production of low-density nanofoams with high thickness (boron and metals). For all these reasons, the choice fell on boron (B), silicon (Si), copper (Cu), tungsten (W), and gold (Au). We first perform a detailed investigation of the effect of the background argon pressure on a subset of the investigated elements (i.e., boron, copper, and tungsten), to study the morphological evolution and define the optimal conditions to produce low density nanofoam films. The obtained insights are then exploited to produce nanofoams of all the elements considered, with special attention to their nanoscale and microscale morphology, density, uniformity, thickness, growth rate, and oxygen content. Then the morphology evolution is discussed, together with the observed differences among the elements, with the help of a simplified model based on the nanoparticle interaction with the background gas atoms. The evolution of the nanofoam average density with the argon pressure is explored in greater detail, corroborating the discussion on the materials morphological features. Finally, a comparison between the elements considered in this work and carbon nanofoams—among the most studied PLD nanofoams—is also performed, revealing the distinctive behavior of carbon.

## 2. Results

Among all the elements investigated in this work, chosen for their different characteristics—varying metallic character, density, atomic number, physical properties—a subset was first

selected to study the effect of the background gas pressure present in the deposition chamber. This is one of the main fs-PLD process parameters, and the most influential in determining the deposited material characteristics, from nanostructure and morphology to average properties like density and uniformity.

## 2.1. Morphological Characterization

Since the nanofoam morphology arises under specific conditions—that is, when the ablated species, slowed by the background gas, aggregate in fractal-like structures before depositing on the substrate<sup>[49,51]</sup>—this analysis can also be exploited to determine if it is possible to produce nanofoams with all the different materials and under which conditions. The effect of the background argon pressure is investigated for boron, copper, and tungsten: a low-, a middle-, and a high-Z element, respectively, one metalloid (B) and two metals (Cu and W) with varied physical and chemical properties. The results of the morphological analysis for each element and background argon pressure are shown in **Figure 1** (top view) and **Figure 2** (cross section). One representative scanning electron microscope (SEM) image is shown for each pressure condition (columns) and each element (rows). In support of the morphological characterization, the average density of each sample is also reported in Figure 1, as the main macroscopic parameter of the nanofoam. A second set of the two images, in which the magnification is kept constant at 5000X for all micrographs, is included in the Supporting Information.

Nanostructured films in which nanoparticles are the basic constituents are obtained in all pressure conditions, from high-vacuum (less than  $10^{-3}$  Pa) up to high-argon pressures (thousands of Pa). By increasing the background pressure, the morphology evolves similarly for all the elements, going from

nanoparticle-assembled compact films to porous nanofoams. In high-vacuum conditions, compact nanoparticle-assembled films are obtained in all cases, consistently with the direct nanoparticle emission typical of the ultrafast ablation process. Both copper and tungsten films are characterized by spherical nanoparticles, with a partially melt appearance (evident from the cross-section images of Figure 2). On the other side, the boron film exhibits less distinguishable and irregularly shaped nanoparticles, leading to a seemingly more compact morphology. Considering the nanostructure of the films, a near-solid density could be expected, reduced in part by the presence of voids in the nanostructure. This is the case for boron, featuring a density of  $1.84 \text{ g cm}^{-3}$  against a bulk density of  $2.3 \text{ g cm}^{-3}$ . Copper and tungsten films present densities of  $4.48$  and  $8.39 \text{ g cm}^{-3}$ , corresponding to approximately half of the respective bulk densities. When low argon pressure is used, as can be appreciated by comparing the copper and tungsten films at  $100 \text{ Pa}$  with those in vacuum conditions, the overall morphology is similar and the density comparable—somewhat decreased for copper and slightly increased for tungsten. The main difference can be found in the films nanostructure: the nanoparticles are smaller on average, and most of the smaller ones aggregate on the surface of the bigger nanoparticles. The morphological features associated to partial melting—typical of the vacuum conditions—are also less predominant, especially for tungsten. The aggregation of the smaller nanoparticles on the surface of the larger ones is more evident in the case of copper, leading to a clear increase in film porosity (and resulting decrease in average density). On the contrary, the tungsten film presents a more compact morphology, less aggregate formation, and a general decrease in average nanoparticle size. The peculiar density increase with increasing pressure for tungsten in these conditions—while small enough to be within the experimental

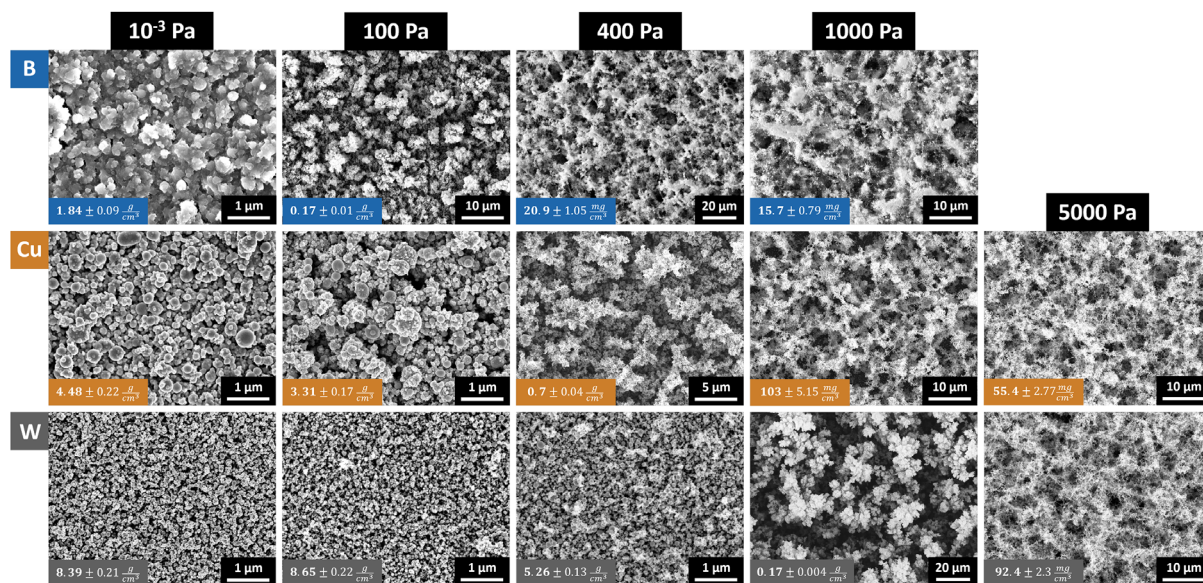


**Figure 1.** Top-view SEM micrographs showing the evolution of film morphology, from vacuum conditions up to  $5000 \text{ Pa}$  background argon pressure (left to right). The corresponding film average density is also reported. Boron films are in the upper panels, copper in the middle, and tungsten in the bottom ones. The respective cross sections are shown in Figure 2. Note that the scale bar is not the same for all images: for each of them, the most appropriate magnification to highlight the main morphological features of the film was chosen.



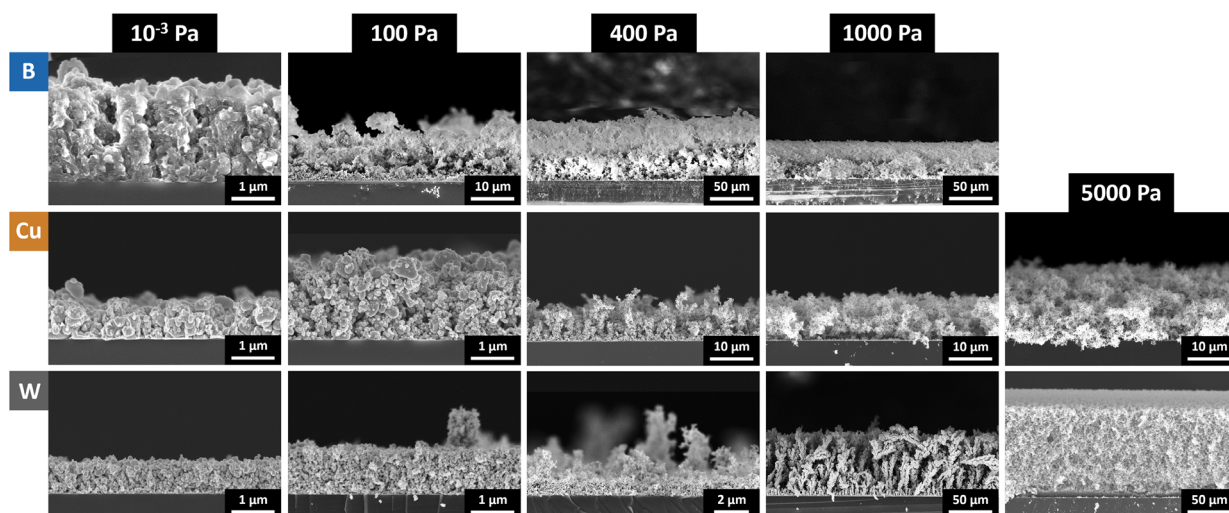


**Figure 2.** Cross-section SEM micrographs showing the evolution of film morphology, from vacuum conditions up to 5000 Pa background argon pressure (left to right). Boron films are in the upper panels, copper in the middle, and tungsten in the bottom ones. The respective top views are shown in Figure 1. Note that the scale bar is not the same for all images, as the most appropriate magnification was chosen for each.

uncertainty—could be the result of a tighter packing due to the smaller nanoparticle size.

Further increasing the pressure leads to a sharp change in morphology, as demonstrated by the tree-like and cauliflower-like morphology of tungsten at 1000 Pa, copper at 400 Pa, or boron at 100 Pa. In these conditions, the growth of the film is largely directional, as reflected in its nanostructure, characterized by more voids of larger size. The resulting density is thus noticeably lower, in the order of  $0.1\text{--}1\text{ g cm}^{-3}$ . The morphology in this pressure range is the most varied and can also simultaneously present features of both compact nanoparticle assembled films and porous aggregates, as can be appreciated from the cross-section images of Figure 2. Moreover, different deposition rates can have a noticeable impact on the tree-like morphologies: the high deposition rate of tungsten is the reason for the emergence of the highly directional tree structures absent in the copper and boron films. Nevertheless, the film morphology remains similar, despite different spatial scales, as can be appreciated from the top-view micrographs of boron at 100 Pa, copper at 400 Pa, and tungsten at 1000 Pa of Figure 1. When even higher argon pressures are reached, in the order of 400 Pa for boron, 1000 Pa for copper, and 5000 Pa for tungsten, the last morphological transition takes place, with the emergence of the nanofoam structure. The morphology is fractal-like, with aggregates formed by strands and clusters of nanoparticles linked together. The resulting void fraction can be higher than 90%, which leads to densities down to  $10\text{--}100\text{ mg cm}^{-3}$ . Interestingly, under these conditions only (i.e., when the pressure is high and a nanofoam material is obtained), it is possible to see some light emission/scattering along the laser path in the PLD chamber (Figure 3), akin to what happens when light travels through vapor. This happens regardless of the target material and could be an indication of the high concentration of ablated species and nanoparticles inside the deposition chamber under those specific conditions. No data was reported for boron samples at 5000 Pa, since under those conditions the plume confinement resulted too high, and

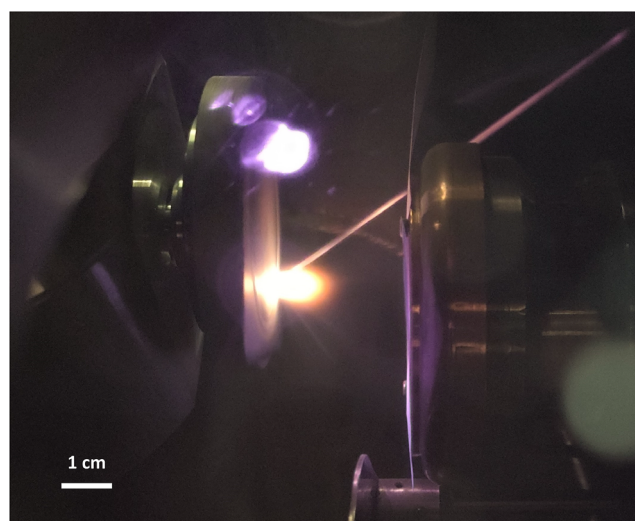


**Figure 3.** Camera picture of the fs-PLD ablation plume, in which the light emission along the laser path can be clearly distinguished. The target is on the left, the substrate on the right, and the laser comes from the back at  $45^\circ$  angle with respect to the target. The target was silicon and the pressure 1000 Pa, the same condition used to obtain the nanofoam of Figure 4. The white bright spot on the top of the image is an optical artifact.

most of the ablated species redeposited in the vicinity of the target and only a small fraction was able to reach the substrate. No film was grown on the substrate in those conditions, only a few single aggregates were present. This detrimental effect resulting from an excessively high pressure is not unexpected and was already observed in our previous work on carbon nanofoams.<sup>[51]</sup>

It is interesting to note that the morphological evolution is analogous for all the elements investigated, going from nanoparticle-assembled compact films in vacuum conditions to tree-like/cauliflower-like morphologies and then nanofoams at higher

pressures. The main difference between elements is the pressure at which these morphological transitions take place, which can vary considerably (e.g., 400 Pa to obtain the boron foam against 5000 Pa for the tungsten one). Moreover, this holds for all the morphological transitions described, as shown in Figure 1 and 2: analogous morphologies are found in films on the top-left to bottom-right diagonal. For example, the intermediate tree-like morphology emerges at 100 Pa for boron, 400 Pa for copper, and 1000 Pa for tungsten. Considering the cross section of the tungsten sample at 5000 Pa in Figure 2, it may appear less porous compared to the nanofoams of other materials. The higher magnification top view of Figure 1 shows the porosity and characteristic nanofoam morphology more clearly, better highlighting the similarities among all the materials. The lower magnification of the cross-section image, together with the high deposition rate of tungsten, is at the origin of the more compact appearance of the tungsten nanofoam in the cross-section micrograph.

The SEM images of Figure 1 are also useful to draw further morphological details, such as nanostructure uniformity at the nano- and microscale. In this context, the nanostructure uniformity is not the macroscale uniformity of the film (i.e., the variation of the film thickness over the film surface) but is related instead to the most predominant spatial scale at which the nanostructure develops. In our previous works we also performed a quantitative analysis of the nanofoams uniformity features, aided by energy-dispersive X-spectroscopy (EDXS) maps and a method based on their Fourier transform.<sup>[26,51,56]</sup> Due to the different properties of the materials investigated in this work (higher-Z elements together with higher density and film thickness), the same approach would not be feasible. Moreover, in our previous works, we showed that the results of the EDXS maps' investigation were in agreement with the qualitative analysis of the nanofoam morphology through SEM micrographs, which is already rich in information and therefore has been chosen as the focus of this investigation. Further qualitative characterizations, such as EDXS maps or laser confocal microscopy (LCM),<sup>[57,58]</sup> are beyond the scope of this work and could be addressed in future studies. In the vacuum samples, all-nanoparticle-assembled films, the uniformity is a direct consequence of the nanoparticles dimensions: the smaller nanoparticles of the tungsten sample lead to the highest uniformity, while copper and boron display larger nanoparticles and a lower uniformity. The morphology of the samples obtained under moderate-pressure conditions is the most varied: it can be closer to tree like in some cases or cauliflower like in others, but the transition between compact and foam-like morphologies is not clear cut, and mixed morphologies can also arise. This is apparent in the cross-section image of the boron sample at 100 Pa (Figure 2), with a more compact tree-like morphology near the substrate on top of which porous cauliflower-like structures grow. The nanostructure uniformity in this intermediate regime remains a result of the specific morphology: the copper sample (400 Pa) is the most uniform, since it is halfway between a compact and a tree-like morphology; boron (100 Pa) is less uniform, with a mixed morphology between tree-like and cauliflower-like; tungsten (1000 Pa) is the least uniform, due to the strongly anisotropic tree-like growth. The different magnifications needed to highlight the main morphological features of those three samples in Figure 1—10 KX for copper, 5 KX for boron, and 2 KX for tungsten—reflect the uniformity

variations. Finally, the nanostructure uniformity is lowest for the nanofoams, due to the larger voids and aggregates forming the material; further increasing the pressure leads to an only minor decrease in uniformity. No substantial variations are observed among the different elements, coherently with the morphological similarities and hinting at an analogous aggregation mechanism.

## 2.2. Thickness Evolution and Deposition Rate

Exploiting the insights gained through the morphological analysis, notably the optimal pressure conditions, we were able to produce nanofoam films from a wider variety of elements. In addition to boron, copper, and tungsten, we have investigated the synthesis of nanofoams of silicon (Si) and gold (Au). These elements are not only interesting *per se* due to their widespread scientific and technological applications, but also because they possess physical characteristics that are complementary with respect to the elements already considered (Si is a low-Z semiconductor, Au is a high-Z noble metal). The nanofoams of boron, copper, and tungsten are obtained at 400, 1000, and 5000 Pa respectively, resulting from the previous analysis. 1000 Pa was also used for silicon and gold. In all cases, the nanofoams display the same distinctive morphology (upper panels of Figure 4): a disordered network of fractal-like structures with significant void fraction (>95%), whose basic constituents are solid nanoparticles from a few to a few hundreds nanometers in diameter.

Despite the morphological similarities at the microscale, interesting variations in nanoparticle sizes and nanoscale morphology can be highlighted among the different elements, as shown in the high-magnification SEM images of the nanofoams (bottom panels of Figure 4). Copper and gold foams both display very well-defined spherical nanoparticles—arranged in chain-like structures or more compact 3D clusters—with a predominance of bigger nanoparticles in the range of 50–200 nm (this effect is more prominent in the case of gold, where the nanoparticle dimension is larger on average). Boron and silicon instead show the typical nanofoam web-like morphology also at lower spatial scales: the larger nanoparticles are present but less predominant, and most of the structure is made up of strands of smaller nanoparticles (10–50 nm), giving rise to the typical “hazy” appearance under the electron microscope. Finally, tungsten shows nanoscale features that are a middle way between the two groups: the nanostructure morphology is quite similar to that of gold and copper, but the nanoparticles are even smaller than boron and silicon and more uniform in size (none is bigger than 50 nm in diameter). The nanofoams of Figure 4 were all obtained with the same fluence conditions—that is,  $110 \text{ mJ cm}^{-2}$  on target—confirming the universal character of the ultrafast ablation mechanism. Moreover, the effective ablation threshold of B, Si, Cu, and W is found to be quite similar, in the range of  $20 \text{ mJ cm}^{-2}$  ( $\approx 18 \text{ mJ cm}^{-2}$  for copper and tungsten,  $\approx 24 \text{ mJ cm}^{-2}$  for boron and  $\approx 26 \text{ mJ cm}^{-2}$  for silicon). Operatively, starting from zero fluence and gradually increasing the laser energy on target, this is the fluence condition in which the ablation plume appears (in vacuum conditions).

The thickness of the nanofoam can be controlled by changing the deposition time accordingly: the deposition rate remains constant with an increase in deposition time (see Figure 5 for boron



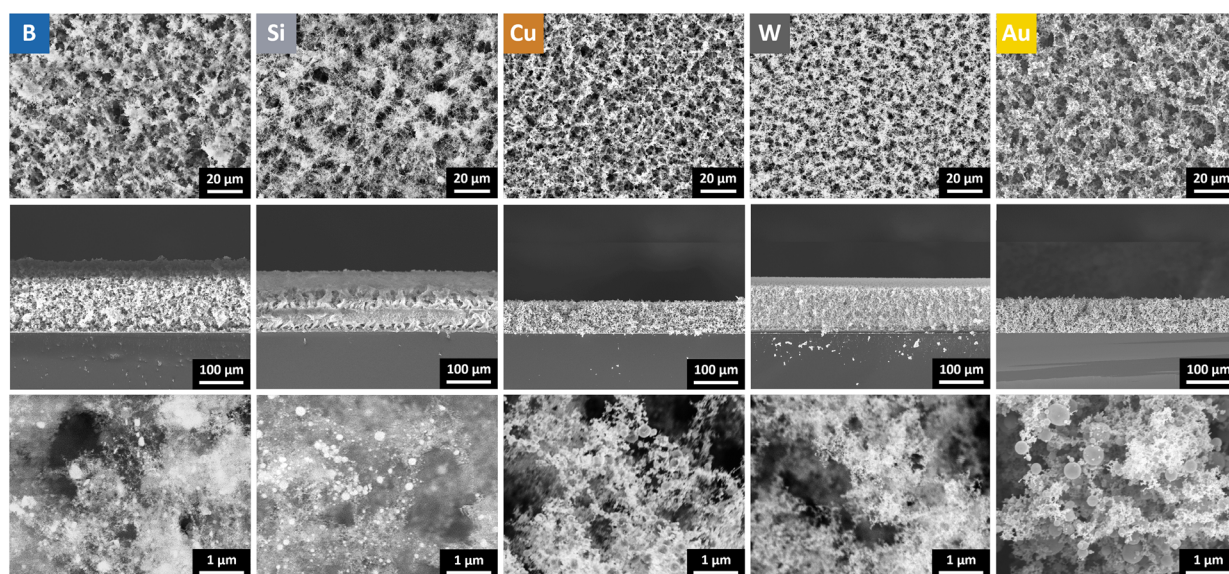


**Figure 4.** SEM micrographs of nanofoam materials of different elements, produced through fs-PLD. Top view is shown in the upper panels, with the corresponding cross-section view right below. Note the foam thickness, close to or surpassing 100  $\mu\text{m}$  in all cases. In the bottom panels, higher magnification images reveal the nanoscale morphology and nanoparticle sizes. All are obtained with a laser fluence of 110  $\text{mJ cm}^{-2}$ , and different background argon pressure: 400 Pa for B, 1000 Pa for Si, Cu e Au, 5000 Pa for W.

and copper) and the density and morphology of the material are largely unaffected.

This holds as long as the nanofoam is thick enough to be able to define a meaningful thickness (and thus density) value. Considering the additive growth mechanism, the first growth stages lead to the formation of separate aggregates on the substrate, and only when enough aggregates deposit on the substrate, the nanofoam structure grows. Therefore, the minimum nanofoam thickness achievable is close to the average aggregate dimension, with incomplete coverage and low uniformity. As long as the foam thickness is a few times higher than the

largest aggregate dimension, a mostly complete coverage and a satisfactory uniformity are reached. Aggregate dimensions are generally in the micrometer range (they can vary according to material properties and deposition conditions). Therefore, the minimum foam thickness is in the order of 5–10  $\mu\text{m}$ . The maximum thickness has no definite upper bound: in principle it is sufficient to increase the deposition time in accordance to the desired thickness. Figure 4 shows that a thickness of 100  $\mu\text{m}$  and above can be readily reached for all the elements considered. It should nevertheless be noted that the mechanical rigidity of the nanofoam is lower to that of a solid material, and it is prone to morphological rearrangements if subjected to vibrations or stresses, effect worsened when the thickness is increased. For all these reasons, an upper limit on foam thickness in the order of a few hundreds of micrometers is expected, above which structural stability problems (e.g., collapsing under its own weight, on-substrate reorganization, and coalescence) might become important.

A high deposition rate is one of the advantages of the fs-PLD technique, thanks to the material removal efficiency of the ultra-fast ablation mechanism. As shown in Figure 5, there is a notable difference in deposition rate among the different materials, which can be roughly divided in two groups: gold and copper have a lower deposition rate, close to 1.1  $\mu\text{m min}^{-1}$ , while all the others—boron, silicon and tungsten—are in the range of 8–10  $\mu\text{m min}^{-1}$  (considering the 1 kHz repetition rate, they correspond to 0.018 and 0.13–0.17  $\text{nm/shot}$  respectively). This same behavior is reflected in the deposition times used to obtain the thick nanofoams of Figure 4: 10 min are enough for silicon and tungsten, 20 are used for boron (resulting in a correspondingly higher foam thickness), and 60 for copper and gold. As mentioned before, the density of the foam is largely unaffected by the deposition time; therefore a linear relationship also holds between deposition time and foam mass thickness; in that case,

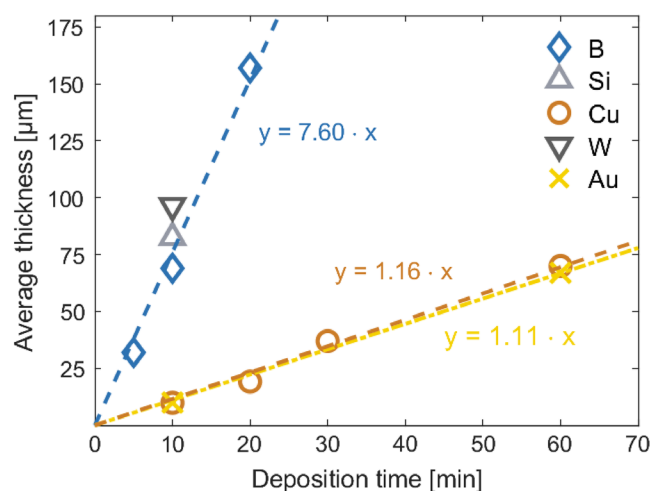


**Figure 5.** Evolution of the foam thickness against the deposition time for boron, copper and gold (linear fit shown). A single point for silicon and tungsten foams at 10 min is shown as comparison. The deposition conditions—beside the deposition time—are the same as in Figure 4.

the specific nanoparticle density also plays an important role, since the foam mass thickness is proportional to the nanoparticle density.

Considering the nanofoam highly porous morphology—and the resulting high surface area-to-volume ratio—some oxygen content is expected to be present, in particular for the materials that can undergo oxidation (copper, tungsten, silicon) and even more if they are efficient oxygen getters such as boron. The oxygen content was consistent in the boron, silicon, and tungsten foams (up to 30% in atoms), lower for copper (less than 10%), and virtually absent for gold foams. As could be expected, the oxygen content of the films is gradually reduced for the more compact films (i.e., those obtained with lower argon pressure). It should be noted that all samples have been exposed to ambient air before oxygen content determination through EDXS. Therefore, applications requiring low oxidation should consider—and benefit from—special care to avoid exposure to air.

A further point worth mentioning, in view of the use of fs-PLD for nanostructured material production, is the macroscale uniformity of the deposition across the substrate, which is one of the main drawbacks of exploiting ultrafast ablation for PLD. The ablation plume is strongly directional,<sup>[38]</sup> leading to a dishomogeneous material deposition on the substrate; reasonable areas to be coated uniformly are in the order of  $5 \times 5$  up to  $10 \times 10$  mm. Nevertheless, the issue is less pronounced for higher pressure deposition (the ablation plume is more confined) and can be further mitigated by increasing the target-to-substrate distance. It is also possible to consider a proper substrate motion routine to compensate for the nonhomogeneous deposition, with the drawback of a reduced deposition rate.

### 3. Discussion

In order to better understand the effect of the background gas pressure on the ablated species, and hence on the related morphological features, it is useful to consider a simplified model of the process. The fs-PLD technique leads mainly to the production of nanoparticles and clusters as ablated species, with dimensions ranging from a few to a few hundred of nanometers.<sup>[39,40,59]</sup> We can consider the ablated species as spheres of radius  $R$  and density  $\rho$ , ejected from the target with a certain velocity  $v$  depending on the specifics of the laser–matter interaction. The nanoparticles then travel toward the substrate and can be slowed by successive collisions with the atoms/molecules of the background gas. With the aid of simple force balance considerations, and in the approximation of elastic scattering events, it can be shown that the ablated species velocity decreases as follows (consistently with the more rigorous derivation of Epstein's relations<sup>[60]</sup>).

$$\dot{v} = -\gamma v, \quad \gamma \propto \frac{P}{R\rho v_t} \quad (1)$$

The factor  $\gamma$ , representative of the slowing efficiency of the background gas on the ablated nanoparticles, is directly proportional to the pressure  $P$  and inversely proportional to the radius and density of the nanoparticles. It is also inversely proportional to the thermal velocity  $v_t$  of the background gas atoms, that is a constant in our experiments.

When the deposition is carried out in vacuum conditions, the ablated nanoparticles are free to travel unrestricted from the target to the substrate, retaining most of their original kinetic energy. A compact film can be expected, still presenting a nanoparticle-assembled morphology coherently with the direct nanoparticle emission typical of the ultrafast ablation process. The partially melt morphology of the metallic films (copper and tungsten) is likely due to the high energy provided by the femtosecond laser to the target material—and thus to the ablated species—leading to the melting of the nanoparticles after they are emitted from the target. They can then solidify on the substrate, explaining the peculiar morphology seen in the cross-section images (Figure 2). In the case of copper, the melting effect appears more pronounced, likely due to the lower melting temperature with respect to tungsten (along with the larger nanoparticle size). The difference in morphology for the boron film—more compact and with angular nanoparticles—could be related to the different response of the target material to the ultrafast ablation between metals and metalloids.

As illustrated by Equation (1), when the pressure is increased the ablated species are progressively slowed, an effect that is greater for nanoparticles with smaller radius and lower density. In real experimental conditions, the nanoparticle density can be considered—as a first approximation—equal to the solid bulk density, while the nanoparticle dimension distribution is in general multidisperse (refer to the bottom panels of Figure 4 for instance). As a consequence, the smaller nanoparticles can be efficiently slowed at lower pressures, while the larger ones are less affected until higher-pressure conditions are reached.

This is related to the morphological transitions seen in Figure 1 and 2: when the argon gas is present but the pressure is low, there are but a few collisions, and most of the nanoparticles still reach the substrate with sufficient energy to give rise to compact films; nevertheless, some of the smaller nanoparticles can be slowed and stick to each other or to the larger nanoparticles, forming small aggregates. This can explain the small changes in morphology seen in the tungsten and copper films at 100 Pa with respect to those obtained in vacuum conditions. By further increasing the gas pressure, even the larger nanoparticles begin to slow, despite not quite reaching a diffusive regime; the residual kinetic energy is enough to ensure a predominant growth directionality along the target/substrate normal, leading to a predominantly ballistic aggregation mechanism.<sup>[61–63]</sup> A few aggregates of intermediate size can also be formed, from the aggregation of the smaller nanoparticles able to reach a diffusive regime at lower pressures. This explains the morphological variety displayed by the samples in moderate pressure conditions: the transition between compact and foam-like morphologies is not clear-cut, and relatively small variations in the gas pressure can lead to significant morphological changes. The reason for this effect can be linked to the slowing effect of the background gas: a relatively low increase in gas pressure—up from vacuum conditions—is at first not enough to sufficiently slow the ablated species, and the morphology does not change significantly. When the pressure is further increased, a greater fraction of the ablated species is slowed, and the morphology of the corresponding film depends on the variability within the distribution of kinetic energy and size among the ablated species. If the variability is low, a sharper morphological transition can be

expected, since most nanoparticles would be slowed under the same pressure conditions. This is the case of tungsten and can be the reason for the emergence of the strongly directional tree-like morphology of the 1000 Pa sample. On the contrary, a higher variability—in which under the same pressure conditions the smaller and less energetic ablated species are slowed to a diffusive regime, others to a ballistic one, and the larger and faster are barely affected—can lead to a mixed morphology, where foam-like aggregates, compact structures, and tree-like morphologies can coexist. This is evident in the 100 Pa boron sample for instance.

A diffusive regime is finally reached by further increasing the background pressure: here both smaller and larger nanoparticles—also thanks to the greater time necessary to reach the substrate in this regime—can efficiently stick to one another while in flight and form the micrometric fractal-like aggregates that are the basic constituents of the low-density nanofoams.<sup>[61]</sup>

Despite the many limitations of the simple model of Equation (1) (in real conditions, the ablated particles are not perfect spheres, they can collide and aggregate with each other, and have a wide distribution of radii and starting velocities), its usefulness lies in the determination of the general functional dependence and thus the parameters that have the most influence on the dynamics of the ablated species, as discussed, namely, the background gas pressure, nanoparticle dimension, and mass density, that in turn determine the material morphological and functional properties.

Their average density is probably the nanofoams' most important macroscopic parameter, as porous materials with a high void fraction. Indeed, this is a crucial parameter in many promising applications, for instance, those related to laser–matter interaction.<sup>[17,18]</sup> **Figure 6a** shows in greater detail the evolution of the nanostructured films density with respect to the argon pressure. The complete behavior is shown for the same elements whose morphology evolution is investigated in depth (boron, copper, and tungsten in Figure 1 and 2); single points corresponding to the density of nanofoams of Figure 4 (1000 Pa) are shown for silicon and gold. The curve for carbon nanofoams from our previous work<sup>[51]</sup> is also replicated here for comparison. The analytical function of Equation (2), the same we proposed in ref. [51] for

the case of carbon, is exploited to model the density evolution for the investigated materials. It is (in log–log scale) a sigmoidal function, well suited to follow the observed sharp density variations. The fitting parameters are the compact film density  $\rho_0$ , the foam density  $\rho_f$ , the pressure  $P_0$  at which the sharp density gradient is found (the center of the sigmoid), and the  $k$  parameter. This is a measure of the gradient of the transition: a higher  $k$  corresponds to a steeper gradient, thus a higher density variation occurring in a lower-pressure range.

$$\rho(P) = \rho_0 \left( \frac{\rho_f}{\rho_0} \right)^{\left[ \frac{Pk}{Pk + P_0^k} \right]} \quad (2)$$

The fit results are shown as dotted lines in Figure 6a, with the corresponding fit parameters in Figure 6b. The density evolution—that is, the experimental data points—is well represented by the fit function, with excellent agreement. Starting from the physical meaning of the four fit parameter ( $k$ ,  $P_0$ ,  $\rho_f$  and  $\rho_0$ ), it is possible to address quantitatively the similarities and differences in material behavior for the various elements.

Taking into account the previous discussion on the morphological characteristics of the films, it is clear that the density is related to the nanostructure morphology. This is not surprising, since the average density is the resulting effect from the nanoparticle dimensions and their arrangement in space (i.e., total void fraction) under the reasonable hypothesis of solid density nanoparticles. The density remains high—in the same order of magnitude as bulk density—as long as the film is nanoparticle assembled and mostly compact (for instance up to 400 Pa for tungsten, 100 Pa for copper, only vacuum conditions for boron) and then decreases sharply for the middle morphologies, before stabilizing on the lowest value for the nanofoams. This same general behavior is found in all the elements investigated.

While the general trend is the same, there are several important differences worth mentioning, related to the fit parameters variations shown in Figure 6b: the first, as noted previously, is related to the pressure at which the morphological transitions take place, which depends on how easily the ablated species are slowed by the background gas. This may results from several

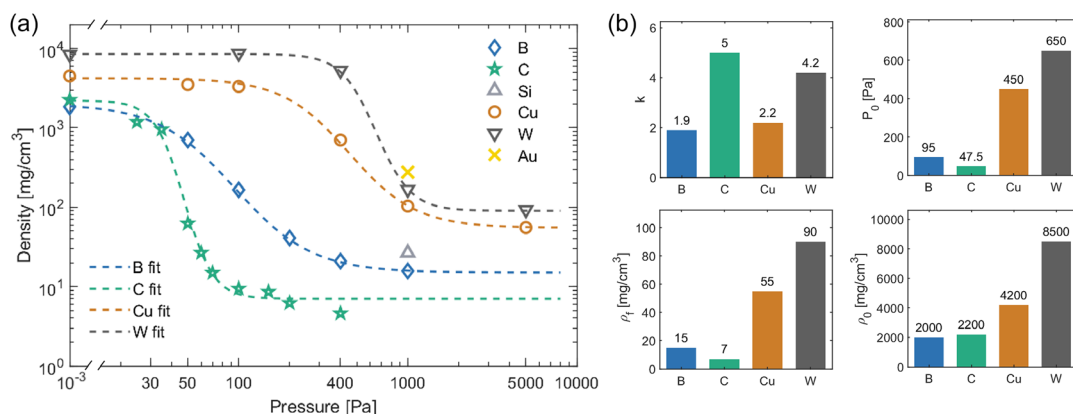


**Figure 6.** a) Density evolution of the nanostructured films as a function of the argon pressure in the PLD deposition chamber. The estimated relative uncertainty for the data points reported is 5% for tungsten, 8% for silicon and 10% for the other materials. The data for carbon is taken from our previous work.<sup>[51]</sup> The dashed lines are fits based on Equation (2). b) Evolution of the fit parameters ( $k$ ,  $P_0$ ,  $\rho_f$  and  $\rho_0$ ) for the different materials considered.



factors, the most important of which—in this study experimental conditions—are the nanoparticle dimension, velocity and density, beside the argon pressure itself (as shown by Equation (1)). In our fit, the associated parameter is  $P_0$ , the center (inflection point) of the sigmoid. More specifically, considering the whole deposition dynamics, this threshold correspond to the pressure at which the majority of the ablated species can be efficiently slowed by the background gas. Between boron and carbon, despite similar bulk densities, a higher  $P_0$  is found for the former, due to the larger nanoparticle size; similarly, the bulk density of tungsten is double that of copper, but the smaller nanoparticle size partially compensate, leading to an only moderate increase in  $P_0$ .

The second difference is related to the nanofoam (or film) density: since all materials have solid nanoparticles as the basic constituents, elements with analogous morphological features but lower (or higher) bulk densities could be expected to present a proportionally lower (or higher)-density film. This under the hypothesis that the nanoparticles density is well approximated with the bulk density of the material, or that the ratio of nanoparticle density over bulk density is the same for all elements. Moreover, this consideration would be strictly valid only if the nanoparticles dimension were the same for all the elements, which is not the case. For instance, the tungsten samples at 1000 and 5000 Pa have a density not much higher than the copper ones, despite the significant gap in bulk densities ( $19.3 \text{ g cm}^{-3}$  against  $8.96 \text{ g cm}^{-3}$ ), while the gold foam at 1000 Pa ( $19.32 \text{ g cm}^{-3}$ ) has higher density than the tungsten one. Both can be explained taking into account the smaller nanoparticle dimension of tungsten compared to copper and gold. All factors considered, the film density is a result of the combined effect of nanoparticles dimension, density, and arrangement in space (i.e., film morphology). Analogously, the density of nanofoam materials of different elements is not constant, as demonstrated by the fit parameter  $\rho_f$ : a higher bulk density leads to a higher nanofoam density, and the same holds true for larger nanoparticle sizes. The behavior of  $\rho_f$  among the different elements thus closely follows that of  $P_0$ , as they both depend in similar ways on nanoparticle density and size.

In the third place, differences in the fit parameter  $k$  can be exploited to obtain insights on the nanoparticle characteristics:  $k$  represents the slope of the sigmoid curve, which in turn determines the pressure interval in which the morphological transition takes place. Taking into account the previous discussion, this can be related to the variation in nanoparticles properties, such as

energy and size distribution. If those properties do not vary significantly—that is, the nanoparticles are close to monodisperse in both energy and dimensions—they are all expected to be slowed to a certain degree under similar pressure conditions. The transition from one morphology to the next would be sharper in this case, with no possibility to give rise to mixed morphologies. This corresponds to a steeper density gradient and thus a higher  $k$ . On the contrary, nanoparticles of a wide range of dimensions and velocities would require different gas pressure conditions to be slowed to a certain degree, and this would lead to a longer transition pressure interval represented by a lower  $k$ . This is also related to the emergence of mixed morphologies. Considering the specific behavior of the elements investigated in Figure 6, the more uniform nanoparticle size distribution for carbon and tungsten would be the reason for their steep morphological variation (high  $k$  parameter); on the other hand, the more gradual density decrease (lower  $k$ ) for boron and copper can be attributed to the presence of nanoparticles of many difference sizes, from tens to hundreds of nanometers.

The comparison with carbon, probably the most investigated element to produce nanofoams with PLD, is particularly interesting from more than one perspective. In Figure 7, the key morphological features of carbon films produced by fs-PLD are shown (for an in-depth discussion, refer to our previous work on the topic<sup>[51]</sup>). The morphology of the carbon nanofoam, in the middle panel, and its nanoscale features (right panel) are not dissimilar from those of the elements investigated in this work (compare with Figure 4). The density dependence on background pressure (Figure 6a) follows the same behavior as the other elements, while being the lowest curve: the density is the lowest at equal pressure, and the pressure required to reach porous morphologies is the lowest. This is consistent with the previous considerations, since graphitic carbon has a density of  $2\text{--}2.2 \text{ g cm}^{-3}$  (close to the boron density) but the nanoparticle dimensions are especially low—less than 10 nm, with virtually no larger nanoparticles.

The most noticeable difference between carbon and the other elements, however, resides in the morphology of the films produced under vacuum conditions: as reported in the left panel of Figure 7, the carbon compact film is uniform, with bulk density, in contrast with the nanoparticle-assembled morphology of all the other elements (Figure 2). This behavior can be attributed to differences in the ablation stage: with the absence of a background gas, a compact film suggests atomic or smaller clusters as ablated species, in contrast to the direct emission

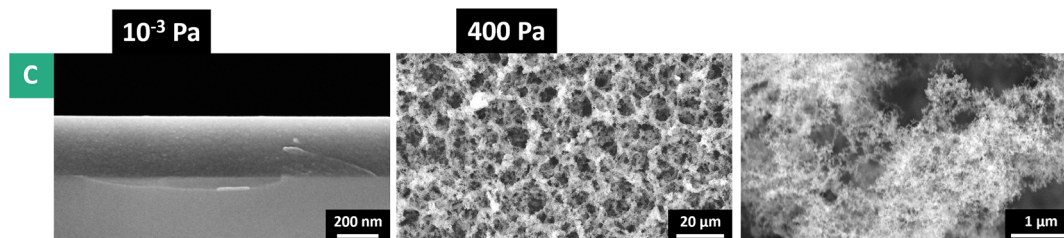


**Figure 7.** Carbon nanofoams produced with fs-PLD (refer to our previous work<sup>[51]</sup> for further details) as comparison to the materials investigated in the present work. In the left panel, the cross-section of a compact carbon film obtained in vacuum conditions is shown; in the middle panel a carbon nanofoam obtained at 400 Pa, and in the lower panel an high magnification image of the same sample, to highlight the nanoscale morphology and nanoparticle features.

of nanoparticles typical of fs-PLD. Incidentally, this can be related to the parameter  $\rho_0$  of Equation (2) and Figure 6, which in the case of carbon is coincident with the material bulk density. Therefore in this case the nanoparticles would need to originate as a consequence of the interaction with the background gas, and this could be the reason for their comparably smaller size. Taking into account the partially melt morphology of the copper and tungsten compact films, and considering the material removal mechanisms in ultrafast ablation, the absence of a liquid phase for carbon (at normal pressure and temperature conditions) could be part of the explanation for the carbon compact film unique behavior.

## 4. Conclusion

For all the elements considered in this work—boron, silicon, copper, tungsten, and gold—nanostructured materials and nanofoams in particular were successfully produced. This was possible thanks to the universal character of the ultrafast ablation mechanism, and its direct emission of nanoparticles, confirming the potential of the fs-PLD technique as a versatile and universal tool for the synthesis of nanofoams with controlled and tunable properties. The typical nanofoam morphology, where nanoparticle-assembled strands connect together to form a web-like fractal structure, was obtained regardless of the element, when the appropriate deposition conditions—that is, background argon pressure—were chosen. The effect of the background pressure, investigated in detail, is indeed shown to be the main driver in determining the film morphology and average density. The reason for this behavior can be found in the interplay between the ablated nanoparticle properties (radius and density) and the slowing effect of the background gas (influenced by the gas pressure and thermal velocity). This is the key to interpret and understand the differences in morphology and density evolution among the elements considered, as well as the link between the nanofoam nanoscale features and macroscopic properties. In doing this, we also show an excellent agreement of a physics-based empirical fit of the average density evolution with the experimental data for all the elements.

The high and constant deposition rate for nanofoams produced by fs-PLD is an ideal feature, allowing to freely control the thickness of the material to suit the specific needs. Together with the density and morphology tunability made possible by suitably adjusting the background gas pressure, it determines the high versatility of the fs-PLD technique, which is not limited to nanofoam morphologies only.

Considering the great interest that nanofoams and nanostructured materials are gathering in many fields of science, it is indeed worthwhile to pursue the development of fs-PLD for nanofoam production. Many questions are still open and would warrant further study, to pursue a greater understanding of the physics at play and better control the produced material properties. Notably, the development of a detailed model of the aggregation and foam growth mechanism, with the aid of computer simulations. A better characterization of the plasma plume, ablated species and nanoparticles would be also especially beneficial for this aim. Considering the ablation process in its entirety, despite the greater modelling challenge, would be also worthwhile, with the final aim of being able to predict the nanofoam

characteristics as a function of the deposition parameters and material properties.

Another relevant development, which will be the focus of further publications, relates to the extension of the study to other elements and their composites, especially those of particular interest for specific applications. In this regard, exploiting the universal character of fs-PLD and performing codeposition of different materials to obtain a mixed-elemental foam is especially promising.

## 5. Experimental Section

The nanofoams in this work were produced through PLD, a well-established physical vapor deposition technique. It exploits a pulsed laser to ablate a target, leading to the formation of an ablated plume that can contain atoms, ions, and clusters, in a vacuum chamber with controlled atmosphere. The ablated species then travel toward a substrate, situated directly in front of the target, on which the material is grown. The presence of a background gas can slow the ablated species, favoring their aggregation, resulting in structural and morphological changes in the produced material. Notably, low-density porous morphologies can lead to higher-background gas pressures. Instead of the nanosecond lasers commonly used in PLD, our setup used a femtosecond laser, a much less explored approach. The potential advantages of fs-PLD arise from the unique characteristics of the ultrafast ablation mechanism (i.e., electronic ablation instead of thermal ablation), which is in principle less dependent on material properties and can lead to direct nanoparticle emission.

Our setup consisted of a commercial Ti:sapphire tabletop laser (Coherent Astrella), with 800 nm center wavelength, pulse duration of  $\approx 80$  fs, 5 mJ per pulse, 1 kHz repetition rate, and 11 mm spot diameter ( $1/e^2$ ). It was focused in the deposition chamber through a 1500 mm focal length lens and impinged on the targets with  $45^\circ$  incidence. Through proper target movement, the laser traced a spiral path on the target, allowing uniform ablation. The fs-PLD experimental setup, composed of the laser system and vacuum chamber, is shown in **Figure 8**. The laser fluence on target was fixed to  $110 \text{ mJ cm}^{-2}$  for all samples, obtained through a laser energy of 3.8 mJ per pulse (or equivalently, 3.8 W average power on target) on 0.88 mm diameter spot. (100) silicon wafer was used as the substrate, and the target-to-substrate distance was kept constant at 3 cm.

Argon was chosen as background gas in the chamber, with pressure ranging from 50 to 5000 Pa. The depositions in vacuum conditions were performed with pressure lower than  $10^{-3}$  Pa. All depositions were carried out in static vacuum. Solid targets of boron, silicon, copper, tungsten, and gold were used. The copper, tungsten, and gold target was metallic with a purity of 99.9%; a (100) silicon wafer was used as silicon target, while the

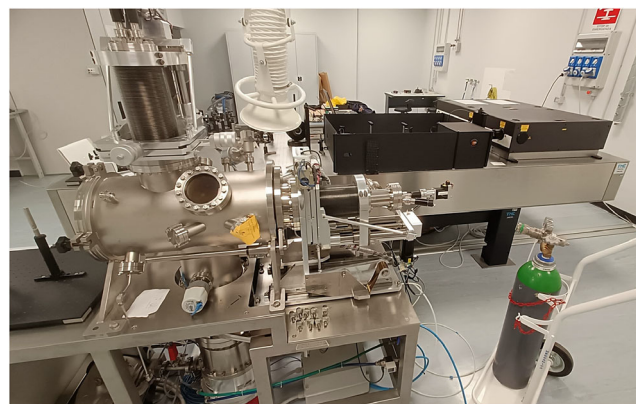


**Figure 8.** The fs-PLD setup at our laboratories.

boron target was sintered and contained some magnesium impurities (<1%).

The morphological characterization exploited SEM, allowing nanostructure and microstructure analysis, both in top view and cross section. A Zeiss Supra 40 field-emission SEM was used, with accelerating voltage of 5 kV. The same electron microscope setup, together with the required X-ray detector, was exploited for energy-dispersive X-ray spectroscopy (EDXS), useful for both elemental composition and density investigation. Regarding this last point, the EDDIE method (EDxs for areal density and composition valuation)<sup>[56]</sup> was exploited to retrieve the foam mass thickness: the characteristic X-ray line intensity for both film and substrate, along with a theoretical model of electron transport and X-ray emission, allowed the determination of the mass thickness. Since the geometrical thickness can be measured in cross-section SEM images, the average density can be calculated as the ratio of mass thickness over geometrical thickness. Operatively, an appropriate SEM electron voltage was chosen (in the range 5–20 kV) in order to have a significant signal for both foam and substrate, and the measure was repeated and averaged over multiple points of the sample. The uncertainty in the average density calculation is largely due to the uncertainties in the physical parameters exploited in the theoretical model of the EDDIE method. From the uncertainty and sensitivity analysis performed with the same accelerating voltages and on samples with comparable properties,<sup>[56]</sup> the mass thickness and density uncertainty was in the order of 10%. For the silicon and tungsten samples, this approach for density determination was not feasible, for similar reasons: the chosen substrate was silicon; therefore, it is not possible to distinguish the characteristic X-rays from the substrate and the film if the element is the same. Tungsten instead happened to have the strongest X-ray signal superimposed to the silicon one (1.74 keV for silicon K line and 1.75 keV for tungsten M line). For these two materials, density determination was performed by weighing the samples before and after the deposition, thus obtaining the nanofoam mass by difference. An analytical balance with a sensitivity of 0.01 mg was used. The substrate dimensions can be measured directly, and the nanofoam thickness was still obtained through SEM cross-section images. The average density was then calculated as total nanofoam mass over average nanofoam volume, with the corresponding uncertainty.

## Supporting Information

Supporting Information is available from the Wiley Online Library or from the author.

## Acknowledgements

This work was carried out within the framework of the EUROfusion Consortium, funded by the European Union via the Euratom Research and Training Programme (grant agreement no. 101052200 — EUROfusion). Views and opinions expressed are however those of the author(s) only and do not necessarily reflect those of the European Union or the European Commission. Neither the European Union nor the European Commission can be held responsible for them. The authors also acknowledge the financial support of the European Union Next Generation EU and Italian Ministry of University and Research as part of the PRIN 2022 program, project “Nanomaterials for Fusion: experimental and modeling of nanostructured materials and plasma-material interactions for inertial & magnetic confinement fusion” (project ID: 2022N5JBHT, CUP D53D23002840006).

## Conflict of Interest

The authors declare no conflict of interest.

## Data Availability Statement

The data that support the findings of this study are available from the corresponding author upon reasonable request.

## Keywords

femtosecond pulsed laser deposition, nanofoams, nanostructured materials, porous materials, pulsed laser deposition

Received: December 18, 2023

Revised: March 17, 2024

Published online: April 16, 2024

- [1] S. Nufer, P. Lynch, M. Cann, M. J. Large, J. P. Salvage, S. Vctor-Román, J. Hernández-Ferrer, A. M. Benito, W. K. Maser, A. Brunton, A. B. Dalton, *ACS Omega* **2018**, *3*, 15134.
- [2] D. Zheng, M. Li, Y. Li, C. Qin, Y. Wang, Z. Wang, *Beilstein J. Nanotechnol.* **2019**, *10*, 281.
- [3] M. B. Sassin, C. P. Hoag, B. T. Willis, N. W. Kucko, D. R. Rolison, J. W. Long, *Nanoscale* **2013**, *5*, 1649.
- [4] H. Zhu, X. Du, Z. Xu, Z. Lin, X. Li, X. Wang, *ACS Appl. Energy Mater.* **2022**, *5*, 7392.
- [5] R. Blinc, D. Arčon, P. Umek, T. Apih, F. Milia, A. V. Rode, *Phys. Status Solidi B* **2007**, *244*, 4308.
- [6] A. S. Thill, D. S. Lima, O. W. Perez-Lopez, R. L. Manfro, M. M. V. M. Souza, D. L. Baptista, B. S. Archanjo, F. Poletto, F. Bernardi, *Mater. Adv.* **2023**, *4*, 476.
- [7] J. Garca-Martnez, T. Lancaster, J. Ying, *Adv. Mater.* **2008**, *20*, 288.
- [8] S. Sun, M. Zheng, P. Cheng, F. Wu, L. Xu, *J. Colloid Interface Sci.* **2022**, *626*, 515.
- [9] L. Chen, S. Zhao, Q.-M. Hasi, X. Luo, C. Zhang, H. Li, A. Li, *Glob. Chall.* **2020**, *4*, 5.
- [10] S. Fu, J. Song, C. Zhu, G.-L. Xu, K. Amine, C. Sun, X. Li, M. H. Engelhard, D. Du, Y. Lin, *Nano Energy* **2018**, *44*, 319.
- [11] R. Gupta, G. U. Kulkarni, *ChemSusChem* **2011**, *4*, 737.
- [12] J. Ma, C. Trellu, N. Oturan, S. Raffy, M. A. Oturan, *Appl. Catal., B* **2022**, *317*, 121736.
- [13] X. Li, J.-F. Tan, Y.-E. Hu, X.-T. Huang, *Mater. Res. Express* **2017**, *4*, 045015.
- [14] S. Kim, D.-H. Cho, H.-K. Chang, H.-N. Lee, H.-J. Kim, T. J. Park, Y. M. Park, *Sens. Actuators, B* **2022**, *358*, 131486.
- [15] I. O. Smith, X. H. Liu, L. A. Smith, P. X. Ma, *WIREs Nanomed. Nanobiotechnol.* **2009**, *1*, 226.
- [16] K. Kupnik, M. Primožič, V. Kokol, M. Leitgeb, *Polymers* **2020**, *12*, 2825.
- [17] M. Passoni, F. Arioli, L. Cialfi, D. Dellasega, L. Fedeli, A. Formenti, A. Giovannelli, A. Maffini, F. Mirani, A. Pazzaglia, A. Tentori, D. Vavassori, M. Zavelani-Rossi, V. Russo, *Plasma Phys. Contrroll. Fusion* **2019**, *62*, 014022.
- [18] M. Passoni, A. Sgattoni, I. Prencipe, L. Fedeli, D. Dellasega, L. Cialfi, I. W. Choi, I. J. Kim, K. A. Janulewicz, H. W. Lee, J. H. Sung, S. K. Lee, C. H. Nam, *Phys. Rev. Accel. Beams* **2016**, *19*, 061301.
- [19] I. Prencipe, A. Sgattoni, D. Dellasega, L. Fedeli, L. Cialfi, I. W. Choi, I. J. Kim, K. A. Janulewicz, K. F. Kakolee, H. W. Lee, J. H. Sung, S. K. Lee, C. H. Nam, M. Passoni, *Plasma Phys. Contrroll. Fusion* **2016**, *58*, 034019.
- [20] I. Prencipe, J. Metzkes-Ng, A. Pazzaglia, C. Bernert, D. Dellasega, L. Fedeli, A. Formenti, M. Garten, T. Kluge, S. Kraft, A. L. Garcia, A. Maffini, L. Obst-Huebl, M. Rehwal, M. Sobiella, K. Zeil, U. Schramm, T. E. Cowan, M. Passoni, *New J. Phys.* **2021**, *23*, 093015.



- [21] A. Maffini, F. Mirani, M. Galbiati, K. Ambrogioni, F. Gatti, M. S. G. D. Magistris, D. Vavassori, D. Orecchia, D. Dellasega, V. Russo, M. Zavelani-Rossi, M. Passoni, *EPJ Tech. Instrum.* **2023**, 10, 1.
- [22] F. Mirani, A. Maffini, M. Passoni, *Phys. Rev. Appl.* **2023**, 19, 4.
- [23] A. Maffini, F. Mirani, A. C. Giovannelli, A. Formenti, M. Passoni, *Front. Phys.* **2023**, 11.
- [24] M. Desselberger, M. Jones, J. Edwards, M. Dunne, O. Willi, *Phys. Rev. Lett.* **1995**, 74, 2961.
- [25] S. Depierreux, C. Labaune, D. Michel, C. Stenz, P. Nicola, M. Grech, G. Riazuelo, S. Weber, C. Riconda, V. Tikhonchuk, P. Loiseau, N. G. Borisenko, W. Nazarov, S. Hüller, D. Pesme, M. Casanova, J. Limpouch, C. Meyer, P. Di-Nicola, R. Wrobel, E. Alozy, P. Romary, G. Thiell, G. Soullié, C. Reverdin, B. Villetle, *Phys. Rev. Lett.* **2009**, 102, 195005.
- [26] A. Maffini, M. Cipriani, D. Orecchia, V. Ciardiello, A. Formenti, F. Consoli, M. Passoni, *Laser Part. Beams* **2023**, 2023, 1.
- [27] Z. Chen, W. Ren, L. Gao, B. Liu, S. Pei, H.-M. Cheng, *Nat. Mater.* **2011**, 10, 424.
- [28] Y. Zhang, X. Sun, *Adv. Mater.* **2007**, 19, 961.
- [29] B. C. Tappan, S. A. Steiner III, E. Dervishi, A. H. Mueller, B. L. Scott, C. Sheehan, E. P. Luther, J. P. Lichthardt, M. R. Dirmy, *ACS Appl. Mater. Interfaces* **2020**, 13, 1204.
- [30] Y. M. Park, S. H. Hwang, H. Lim, H.-N. Lee, H.-J. Kim, *Chem. Mater.* **2020**, 33, 205.
- [31] Y. Tokudome, K. Fujita, K. Nakanishi, K. Miura, K. Hirao, *Chem. Mater.* **2007**, 19, 3393.
- [32] C. Forest, P. Chaumont, P. Cassagnau, B. Swoboda, P. Sonntag, *Prog. Polym. Sci.* **2015**, 41, 122.
- [33] V. Diesen, C. W. Dunnill, J. C. Bear, S. Firth, M. Jonsson, I. P. Parkin, *Chem. Vap. Depos.* **2014**, 20, 91.
- [34] L. Mascaretti, A. Nioiretini, B. R. Bricchi, M. Ghidelli, A. Naldoni, S. Caramori, A. Li Bassi, S. Berardi, *ACS Appl. Energy Mater.* **2020**, 3, 4658.
- [35] A. Bailini, F. Di Fonzo, M. Fusi, C. S. Casari, A. L. Bassi, V. Russo, A. Baserga, C. E. Bottani, *Appl. Surface Sci.* **2007**, 253, 8130.
- [36] A. Zani, D. Dellasega, V. Russo, M. Passoni, *Carbon* **2013**, 56, 358.
- [37] B. Rethfeld, D. S. Ivanov, M. E. Garcia, S. I. Anisimov, *J. Phys. D: Appl. Phys.* **2017**, 50, 193001.
- [38] S. S. Harilal, J. R. Freeman, P. K. Diwakar, A. Hassanein, in *Laser-Induced Breakdown Spectroscopy*, Springer, Berlin **2014**, pp. 143–166.
- [39] M. Lenner, A. Kaplan, C. Huchon, R. E. Palmer, *Phys. Rev. B* **2009**, 79, 184105.
- [40] J. Perrière, C. Boulmer-Leborgne, R. Benzerga, S. Tricot, *J. Phys. D: Appl. Phys.* **2007**, 40, 7069.
- [41] J. Winter, M. Spellauge, J. Hermann, C. Eulenkamp, H. P. Huber, M. Schmidt, *Opt. Express* **2021**, 29, 14561.
- [42] S. Ameer-Beg, W. Perrie, S. Rathbone, J. Wright, W. Weaver, H. Champoux, *Appl. Surface Sci.* **1998**, 127, 875.
- [43] A. Zoubir, L. Shah, K. Richardson, M. Richardson, *Appl. Phys. A* **2003**, 77, 311.
- [44] Z. Lin, M. Hong, *Ultrafast Sci.* **2021**, 2021, 9783514.
- [45] K. Yin, Z. Wu, J. Wu, Z. Zhu, F. Zhang, J.-A. Duan, *Appl. Phys. Lett.* **2021**, 118, 21.
- [46] J. Pei, K. Yin, T. Wu, L. Wang, Q. Deng, Y. Huang, K. Wang, C. J. Arnusch, *Nanoscale* **2023**, 15, 15708.
- [47] R. Teghil, L. D'Alessio, A. De Bonis, A. Galasso, P. Villani, A. Santagata, *Thin Solid Films* **2006**, 515, 1411.
- [48] G. Bulai, O. Pompilian, S. Gurlui, P. Nemec, V. Nazabal, N. Cimpoesu, B. Chazallon, C. Focsa, *Nanomaterials* **2019**, 9, 676.
- [49] A. Maffini, A. Pazzaglia, D. Dellasega, V. Russo, M. Passoni, *Phys. Rev. Mater.* **2019**, 3, 083404.
- [50] A. Maffini, A. Pazzaglia, D. Dellasega, V. Russo, M. Passoni, in *Nanoporous Carbons for Soft and Flexible Energy Devices*, Springer, Berlin **2022**, pp. 135–157.
- [51] A. Maffini, D. Orecchia, A. Pazzaglia, M. Zavelani-Rossi, M. Passoni, *Appl. Surf. Sci.* **2022**, 599, 153859.
- [52] L. Giuffrida, F. Belloni, D. Margarone, G. Petringa, G. Milluzzo, V. Scuderi, A. Velyhan, M. Rosinski, A. Picciotto, M. Kucharik, J. Dostal, R. Dudzak, J. Krasa, V. Istokskiaia, R. Catalano, S. Tudisco, C. Verona, K. Jungwirth, P. Bellutti, G. Korn, G. A. P. Cirrone, *Phys. Rev. E* **2020**, 101, 013204.
- [53] R. Craxton, K. Anderson, T. Boehly, V. Goncharov, D. Harding, J. Knauer, R. McCrory, P. McKenty, D. Meyerhofer, J. Myatt, A. J. Schmitt, J. D. Sethian, R. W. Short, S. Skupsky, W. Theobald, W. L. Kruer, K. Tanaka, R. Betti, T. J. B. Collins, J. A. Delettrez, S. X. Hu, J. A. Marozas, A. V. Maximov, D. T. Michel, P. B. Radha, S. P. Regan, T. C. Sangster, W. Seka, A. A. Solodov, J. M. Soures, et al., *Phys. Plasmas* **2015**, 22, 11.
- [54] S. Li, M. Li, Y. Ni, *Appl. Catal., B* **2020**, 268, 118392.
- [55] S. Sharafat, N. M. Ghoniem, M. Anderson, B. Williams, J. Blanchard, L. Snead, The HAPL Team, *J. Nucl. Mater.* **2005**, 347, 217.
- [56] A. Pazzaglia, A. Maffini, D. Dellasega, A. Lamperti, M. Passoni, *Mater. Charact.* **2019**, 153, 92.
- [57] L. Wang, K. Yin, Q. Deng, Q. Huang, J. He, J.-A. Duan, *Adv. Sci.* **2022**, 9, 2204891.
- [58] Q. Huang, K. Yin, L. Wang, Q. Deng, C. J. Arnusch, *Nanoscale* **2023**, 15, 11247.
- [59] R. Teghil, L. D'Alessio, A. De Bonis, A. Galasso, N. Ibris, A. M. Salvi, A. Santagata, P. Villani, *J. Phys. Chem. A* **2009**, 113, 14969.
- [60] P. S. Epstein, *Phys. Rev.* **1924**, 23, 710.
- [61] T. Vicsek, *Fractal Growth Phenomena*, World Scientific, Singapore **1992**.
- [62] P. Meakin, *J. Phys. A: Math. Gen.* **1987**, 20, L1113.
- [63] A. Limaye, R. Amritkar, *Phys. Rev. A* **1986**, 34, 5085.